Prediction and Synthesis of a Selenide Perovskite for Optoelectronics

Han Zhang,[1,2,‡] Xiaowei Wu,[1,‡] Keda Ding,[1,2] Li Xie,[1,2] Ke Yang,[3] Chen Ming,[1,] Shengqiang Bai,[1] Hao Zeng,[4] Shengbai Zhang,[3] and Yi-Yang Sun[1,*]*

[1]State Key Laboratory of High Performance Ceramics and Superfine Microstructure, Shanghai Institute of Ceramics, Chinese Academy of Sciences, Shanghai, 201899, China

[2]Center of Materials Science and Optoelectronics Engineering, University of Chinese Academy of Sciences, Beijing 100049, China

[3]Department of Physics, Applied Physics and Astronomy, Rensselaer Polytechnic Institute, Troy, New York 12180, USA

[4]Department of Physics, University at Buffalo, The State University of New York, Buffalo, New York 14260, USA

Corresponding Author

*E-mail: yysun@mail.sic.ac.cn (Yi-Yang Sun), mingchen@mail.sic.ac.cn (Chen Ming)

ABSTRACT The advent of halide perovskites in recent years opens an avenue of redeveloping perovskite materials as semiconductors. In the quest for semiconducting perovskites, chalcogenides, which exhibit higher stability than their halide siblings and often direct band gaps for optoelectronics, have attracted more and more attention. So far, functional chalcogenide perovskites have been exclusively sulfides. Here, employing first-principles calculations and the criterion of phase stability besides the commonly used thermodynamic and dynamical criteria, we precisely predict the existence of $LaScSe_3$ as a thermodynamically stable selenide perovskite, which is validated by our experimental synthesis. Combining hybrid functional and many-body quasi-particle (G_0W_0 and Bethe-Salpeter equation) calculations, we predict that $LaScSe_3$ is a direct-gap semiconductor having the band gap in the green to blue region and capable of p- and n-type bipolar doping, holding great promise for optoelectronic applications.

1. Introduction

Perovskite materials represent one of the largest families of inorganic functional materials with important applications, such as piezoelectrics, ferroelectrics, multiferroics, photovoltaics, and optoelectronics.[1–5] Oxides contribute to the majority of existing perovskite materials, which have been widely used for dielectric applications. In the past decade, halide perovskites have emerged as attractive semiconducting materials.[5–11] Recently, chalcogenide perovskites have been proposed for various applications.[12–15] As photovoltaic materials, the chalcogenide perovskites could possess more suitable band gaps than their oxide counterparts and are more stable than their halide siblings.[12, 16–19] It has been experimentally demonstrated that perovskite $SrHrS_3$ could yield intense luminescence and potentially fill the so-called "green gap" in light-emitting devices (LEDs).[20] Currently, group-III nitrides have been dominating the applications in LEDs. But they still suffer from issues such as quantum-confined Stark effect,[21] which is originated from the built-in electric field due to the polar nature of the crystal structure. Besides the group-III nitrides, halide perovskites have been intensively studied for LED applications. The external quantum efficiencies of red and green LEDs based on halide perovskites have achieved 25.8% and 28.9%,[22,23] respectively, but the maximum efficiency of blue halide perovskite LEDs of 15.6% [24] is still low, which is probably due to the fact that obtaining blue emission requires the perovskites with mixed Cl–Br anions that tend to segregate into Cl- and Br-rich domains at high applied bias. On the other hand, the short lifetime of halide perovskite LEDs is also a bottleneck for commercial applications.[25] It is thus of great interest to develop the chalcogenide perovskites as a novel family of materials for optoelectronic applications.[26]

The II-IV chalcogenide perovskites ABS_3 with A=Ca, Sr or Ba and B=Zr or Hf are the most widely studied so far.[12, 16–18,27–30] Further enriching the family could be achieved by exploring

other groups of elements at both the cation and anion sites. III-III-S_3 perovskites were synthesized about half century ago,[31] but have not been considered as functional materials. On the anion side, the chalcogenide perovskites are different from halide perovskites. The anions in halide perovskites can be any of the group-VII elements (i.e., F, Cl, Br and I).[5, 32–34] In contrast, chalcogenide perovskites are dominated by sulfides, which have been synthesized since 1956[35] with about 30 reported compounds as collected in the Inorganic Crystal Structure Database (ICSD).[36] Only four uranium-based selenides, namely, $UBSe_3$ with B=V, Cr, Co, and Ni, are reported to exist in the perovskite structure.[37] For functional materials with optoelectronic applications, it is desirable to discover selenide perovskites made of non-radiative elements.

In this paper, we carry out a search for selenide perovskites. By considering I-V-Se_3, II-IV-Se_3 and III-III-Se_3 compounds, we find that $LaScSe_3$ can pass our computational screening on stability checks. We validate the prediction by synthesizing $LaScSe_3$ with solid-phase reaction, as characterized by XRD refined structure, which is in good agreement with the predicted perovskite structure. By hybrid functional and many-body quasi-particle (G_0W_0 and Bethe-Salpeter equation) calculations, we further predict that $LaScSe_3$ possesses a suitable direct band gap for green-to-blue light emission and both p-type and n-type doping are achievable with balanced effective masses of electrons and holes. Our work thus demonstrates an example of precise prediction and realization of a hitherto nonexistent material.

2. Computational and Experimental Methods

The first-principles calculation was based on the density functional theory (DFT) as implemented in the VASP program.[38] Projector augmented wave (PAW) potentials[39] were used to describe the core-valence interaction. Planewaves with kinetic energy up to 340 eV were used. PBEsol functional[40] was adopted in the high-throughput screening calculations, molecular

dynamics simulations and phonon calculations. To tolerate calculation errors, we allowed the energy of other structures to be higher than the perovskite structure by 0.04 eV/f.u. For the materials passing the phase stability check, we adopted the SCAN functional[41] to carry out a final check. We found that the lattice constants obtained from SCAN functional agree better with experimental values than those from the PBEsol functional based on our benchmark with known sulfide perovskites. Therefore, our HSE, G_0W_0 and Bethe-Salpeter Equation (BSE) calculations on band structure and optical properties were all based on the SCAN-optimized structure. The atomic structures were relaxed until the residual forces on all atoms were smaller than 0.0025 eV/Å. Brillouin zone sampling was conducted with a 3×2×3 k-point grid in high-throughput screening calculations, while the optical properties by HSE, G_0W_0 and BSE were obtained using a 7×5×7 k-point grid. In G_0W_0 calculation, 960 bands (80 occupied) were used, which ensure that the calculated band gap is converged to within 0.01 eV. In BSE calculations, 8 top valence bands and 8 bottom conduction bands were included, which was checked to be sufficient. However, the calculated exciton binding energy is still not fully converged with the 7×5×7 k-point grid.

The phonon spectra at 0 K was calculated based on the finite displacement method as implemented in PHONOPY package.[42] A 2×1×2 supercell was used in second-order force constant calculations. The phonon spectra at finite temperatures were calculated by the temperature dependent effective potential (TDEP) method.[43] Ab initio molecular dynamics (AIMD) simulation with an *NVT* ensemble at 300 K was performed by VASP. A 2×2×2 supercell was used. Brillouin zone was represented by the Γ point only. Plane-wave cutoff energy was set to be 238 eV. The simulation was run for 50 ps with a time step of 2 fs. The force constants were extracted from the simulations in the last 40 ps.

$LaScSe_3$ polycrystalline was synthesized by the two-step solid-phase reaction method. Stoichiometric amount of La (99.9%), Sc (99.9%) and Se (99.99%) were mixed and pre-sintered in an evacuated quartz tube at 1100 °C for 3 days. The obtained product was then grinded sufficiently and pressed into pellet in an argon-filled glove-box. The pellet was sintered at 1150 °C in an evacuated quartz tube for another 3 days, followed by furnace cooling to room temperature. The phase composition was characterized by powder X-ray diffraction (XRD) at room temperature using Bruker D8 advance X-ray diffractometer with Cu Kα radiation. The structure refinement was carried out by the JANA2006 package.[44]

3. Result and Discussion

Our approach to discovering selenide perovskites is illustrated in Figure 1. Other than the commonly used thermodynamic and dynamical criteria, the candidate compounds are first subjected to a sieving step to check their phase stability. To pass the check, the calculated total energy per formula unit (f.u.) in the perovskite structure is required to be lower than that in other structures. We considered the $BaSnS_3$, $UFeS_3$, $BaTiS_3$, $CuTaS_3$, $CeTmS_3$, $InAlS_3$, $LaGaS_3$ and $PbGeS_3$ structures (see Figure 1). The criterion for selecting a competing structure is that it has at least two corresponding sulfide compounds in the ICSD. Note that employing the step of phase stability check is not intended to exhaust the possibilities of competing structures, but to make the prediction more targeted. Indeed, if one targets on the discovery of thermodynamically stable compounds, our results suggest that the phase stability check could make the prediction more reliable.

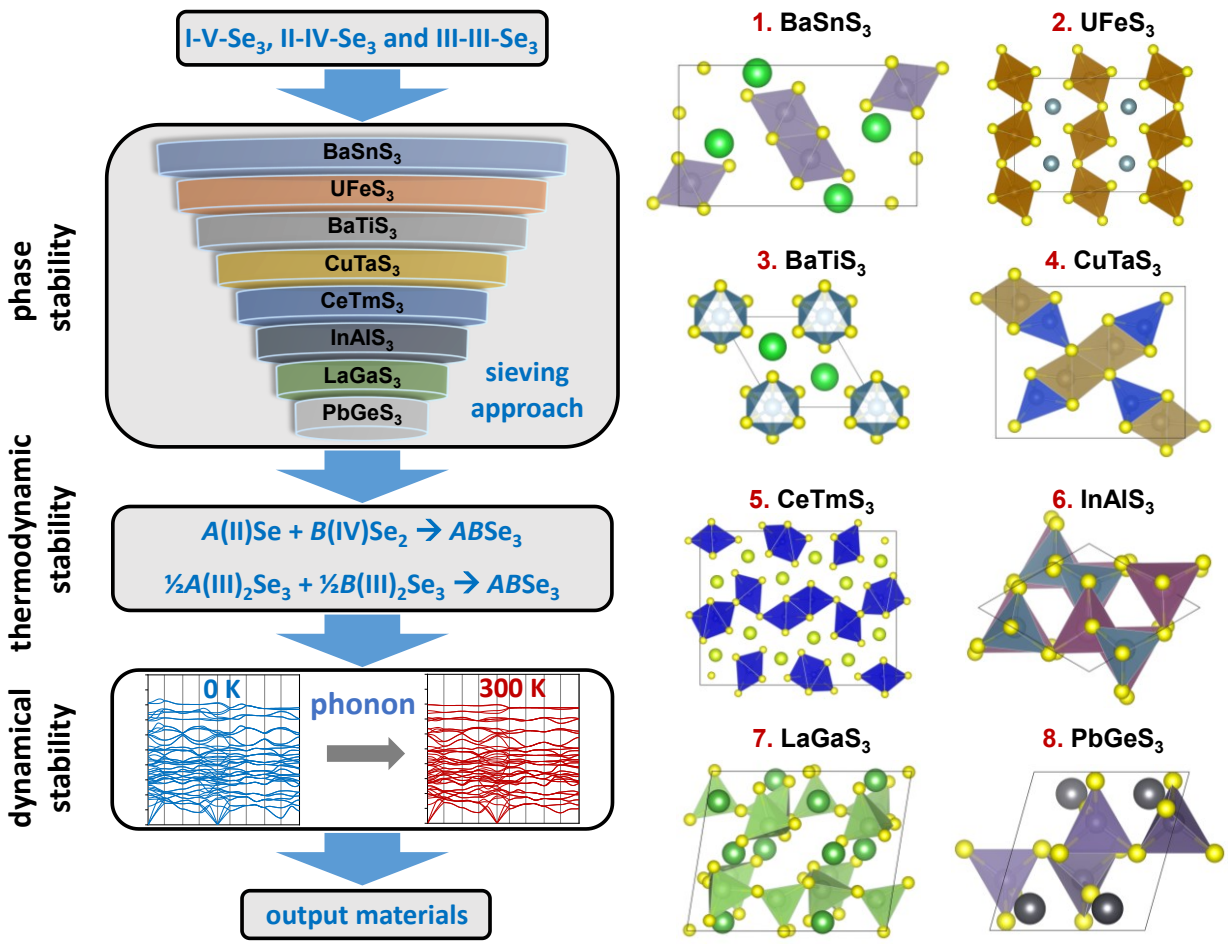

Figure 1. Illustration of the process searching for the stable selenide perovskite materials, including checks on phase stability, thermodynamic stability and dynamical stability. The right panel shows the eight competing structures used for the phase stability check.

We focused on three groups of compounds, namely, I-V-Se_3, II-IV-Se_3 and III-III-Se_3. For the valence-I, valence-II and valence-III cations on the A-site, we considered nine elements each. For valence-V, valence-IV and valence-III cations on the B-site, we considered three, six and nine elements, respectively. The combinations of the elements are shown in Figure 2. For the perovskite structure, it typically requires that the A-site has larger ionic radius than the B-site. So, when the A-site is smaller than the B-site cation, we also switched the two sites and double-checked the stability. Most of the compounds fail in competing with the $BaSnS_3$ structure (labeled as structure

1 in Figures 1 and 2). Another two competitive structures are of $UFeS_3$ (structure 2) and $CuTaS_3$ (structure 4). From Figure 2, it can be seen that the phase stability is a strict criterion. Only two compounds, $LaScSe_3$ and $LuScSe_3$, passed this sieving step.

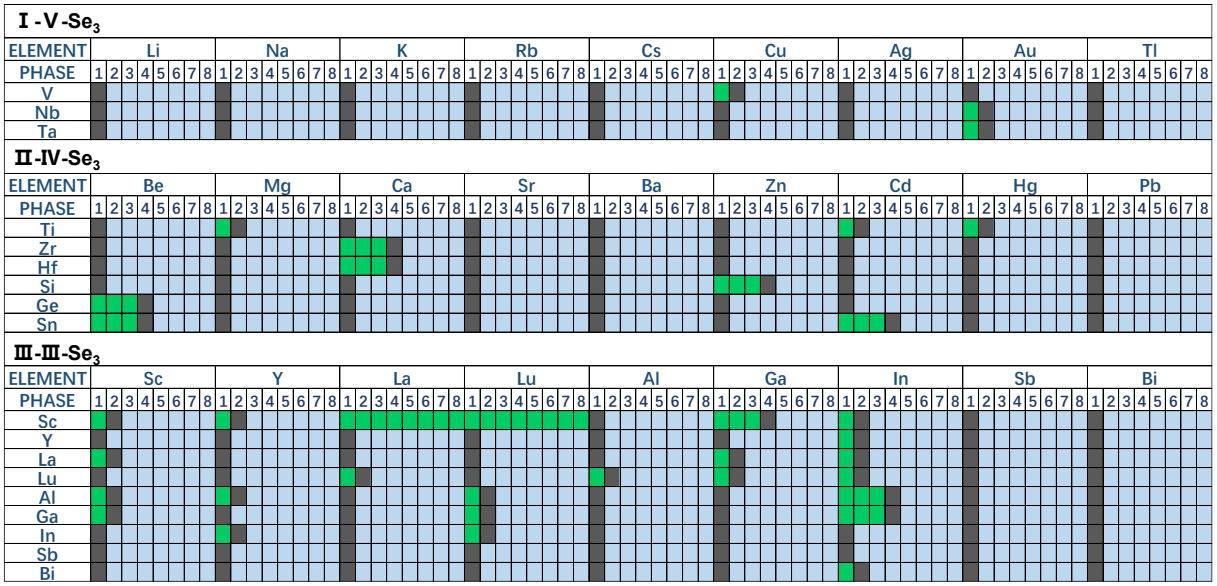

Figure 2. Phase stability for $ABSe_3$ compounds. The A elements are horizontally ordered and the B elements are vertically ordered. The compounds are classified into three groups, I-V-Se_3, II-IV-Se_3 and III-III-Se_3. The eight structures as indexed in Figure 1 are compared with the perovskite structure in total energy. A green grid indicates that the corresponding compound is more stable in the perovskite structure than in the structure under examination. A gray grid indicates the opposite. A cyan grid means that the structure is unnecessary to check. PBEsol functional was used in the phase stability check.

To check the thermodynamic stability against decomposition, we calculated the enthalpy of formation according to

$$\tfrac{1}{2}A_2Se_3 + \tfrac{1}{2}B_2Se_3 \rightarrow ABSe_3$$

for the two III-III-Se_3 compounds passing the phase stability check. We evaluated the stability of La_2Se_3, Lu_2Se_3 and Sc_2Se_3 in possible structures as collected in the ICSD. It is found that La_2Se_3 is the most stable in a structure with space group *Pnma* (No. 62).[45] Lu_2Se_3 and Sc_2Se_3 are the most stable in an orthorhombic structure with space group *Fddd* (No. 70).[46] The calculated enthalpy of formation (ΔH) of $LuScSe_3$ is 0.30 eV/f.u as shown in Figure 3a. The positive value indicates that the ternary compound is thermodynamically unstable with respect to the binary compounds. In contrast, the ΔH of $LaScSe_3$ is still negative and the most stable phase is also in the perovskite structure.

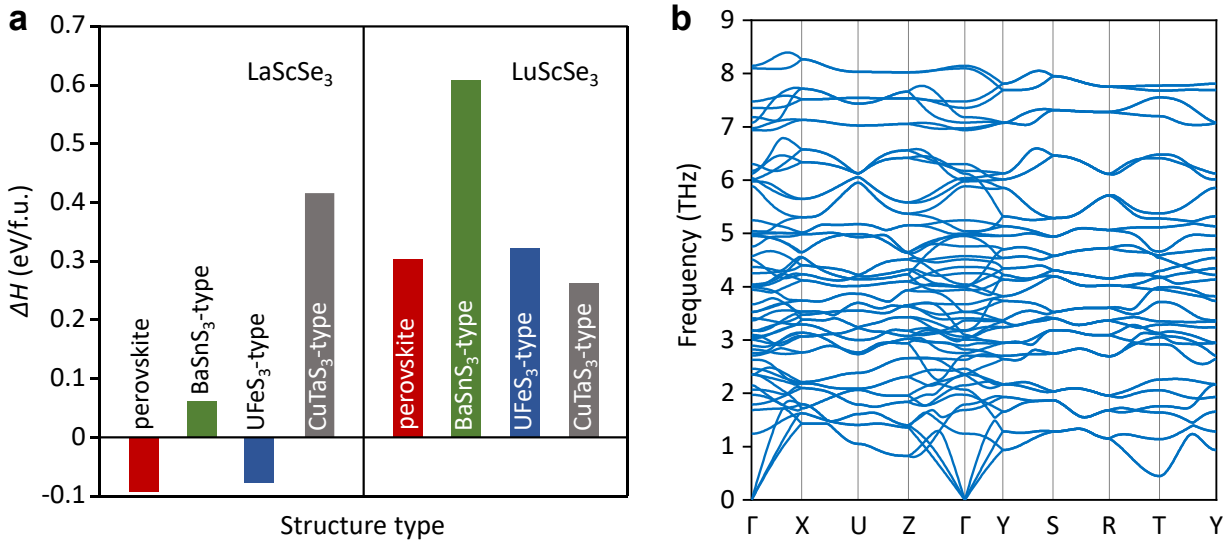

Figure 3. (a) Calculated enthalpy of formation for $LaScSe_3$ and $LuScSe_3$ in the perovskite structure and three major competing structures. More accurate SCAN functional was used in these calculations. (b) Calculated phonon spectrum of $LaScSe_3$ at 0 K. The PBEsol functional was used in this calculation.

Finally, we consider the dynamical stability. Figure 3b shows the calculated phonon spectrum for $LaScSe_3$ at 0 K. No imaginary modes are observed in the spectrum, suggesting its dynamical stability. To evaluate the stability at higher temperatures, we carried out molecular dynamics (MD)

simulations at 300, 600, 900 and 1200 K, as shown in Figure S1 in the Supporting Information (SI). When temperature is increased, the highest-frequency modes become softened, i.e., the frequencies decrease. Usually, the soft modes close to zero indicate the direction of phase change. Interestingly, some of the low-frequency modes, especially the lowest modes at the Z and T points, do not become softer with increasing temperature suggesting that the dynamical stability of $LaScSe_3$ remains even at the high temperatures.

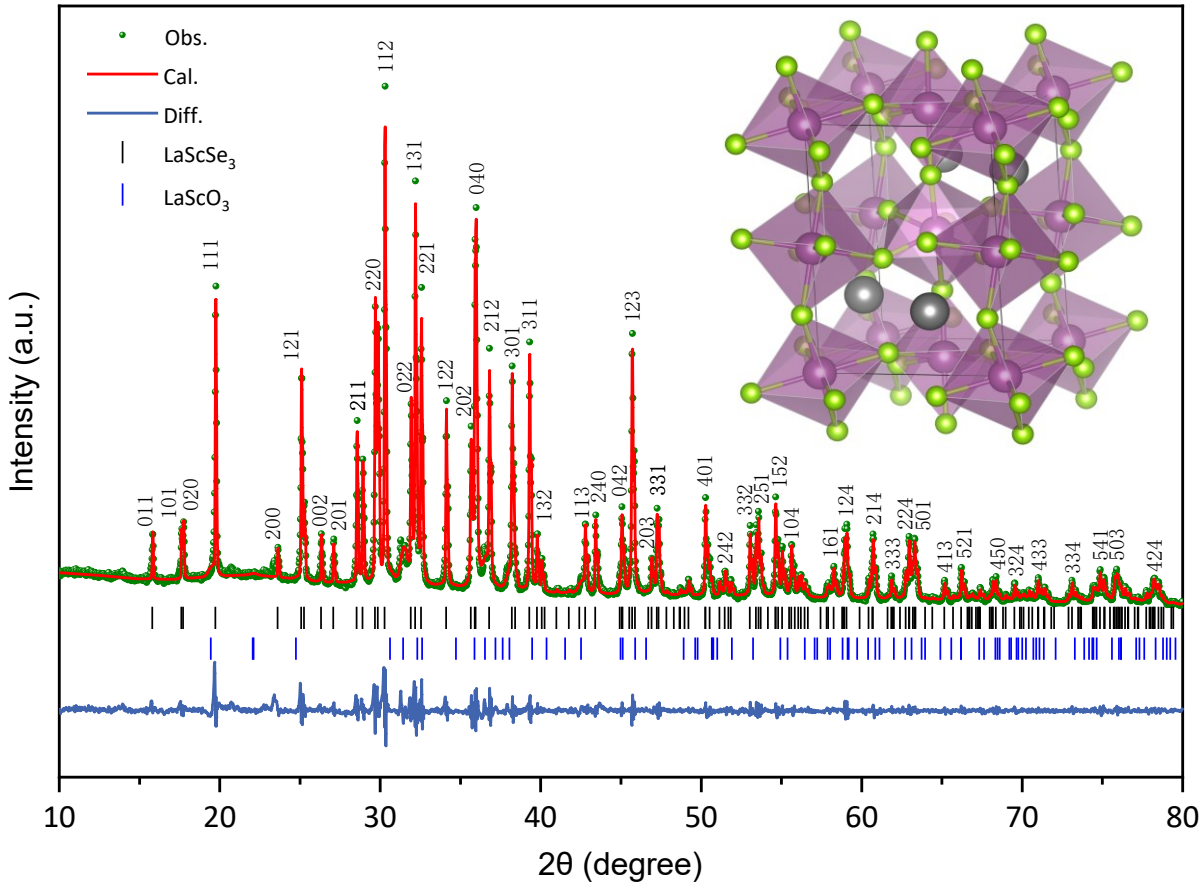

Figure 4. Rietveld refinement of $LaScSe_3$ structure with X-ray diffraction. Two phases $LaScSe_3$ and $LaScO_3$ are considered. The inset shows the refined structure.

By passing the strict screening process, $LaScSe_3$ is the most possible to be synthesized experimentally. To verify the theoretical prediction, we adopted solid-state reaction to synthesize

$LaScSe_3$, as detailed in the SI. The inset of Figure 4 shows the atomic structure of the $LaScSe_3$, which has the *Pnma* space group, the same as the II-IV sulfide perovskites.[47] The corner-sharing octahedra can be clearly seen from the structure. The experimental XRD pattern from the powders are shown in Figure 4. Using the calculated structure as initial values, we carried out multiphase Rietveld refinement by considering the co-existence of $LaScO_3$. The result suggests that the mass ratio of $LaScSe_3$ to $LaScO_3$ is 93.7:6.3. The obtained lattice constants and internal parameters are listed in Table 1 in the SI. With the excellent agreement, we are confident that we have for the first time obtained a non-uranium-based selenide perovskite material. We also compared the experimental XRD pattern with the simulated pattern from the calculated structure. The good agreement, as shown in Figure S2 in the SI, suggests that the calculation method is sufficiently accurate to predict the structure.

We then proceed to discuss the optoelectronic properties of $LaScSe_3$. Figure 5a shows the calculated band structure using the HSE functional.[48] The labels of the high-symmetry points in the Brillouin zone are illustrated in the inset. The material exhibits a direct band gap at the zone center (Γ point). The calculated band gap value (E_g) is 2.28 eV. By including the SOC effect, the VBM is pushed up by about 0.12 eV reducing E_g to 2.16 eV. The decomposed band structures as shown in Figure S3 in the SI indicate that the bottom conduction band and the top valence band are mainly composed of Sc 3d and Se 4p orbitals, respectively.

We also employed the G_0W_0 method to evaluate E_g. Excitonic effect was included by solving the Bethe-Salpeter equation (BSE) to calculate the binding energy of the lowest exciton.[49,50] The quasi-particle G_0W_0 gap is calculated to be 2.96 eV. The BSE calculation shows that the lowest exciton is bright, i.e., the transition from the VBM to the CBM states is allowed. The associated exciton binding energy is 0.17 eV. We calculated the imaginary part of the dielectric constant (ε_2)

of $LaScSe_3$ using different methods, as shown in Figure S4 in the SI. The sharp increase of ε_2 immediately after the band gap manifests the direct nature of the band gap. Considering the SOC correction and the exciton binding energy, the estimated optical gap of $LaScSe_3$ from the G_0W_0-BSE calculation is 2.79 eV.

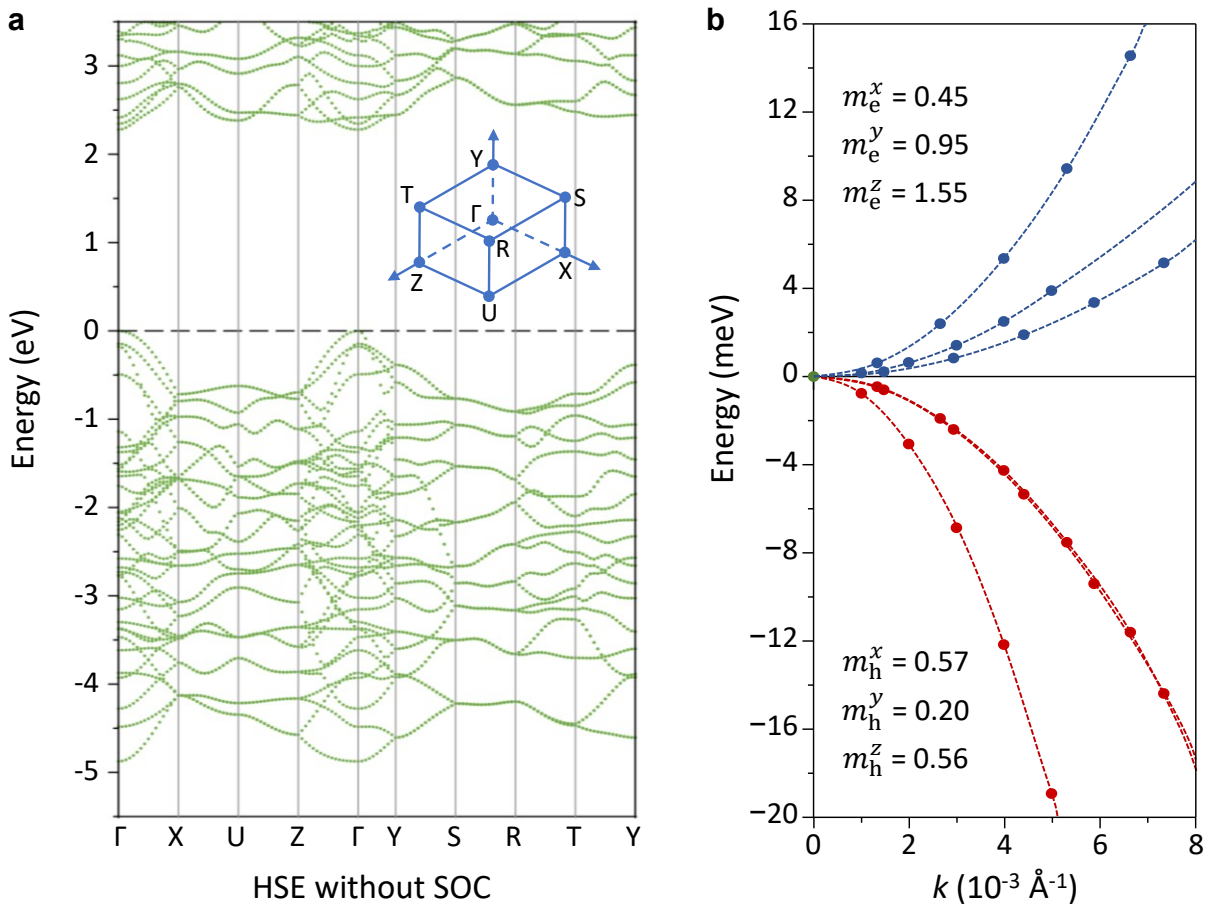

Figure 5. (a) Calculated band structure of $LaScSe_3$ using HSE functional. The inset shows the high-symmetry point in the first Brillouin zone. (b) Parabolic fitting of band structure near the band edges at the Γ point to obtain the effective masses (given as insets). For clarity, the VBM and CBM are taken as the energy zeros for the valence and conduction bands, respectively. Note that the SOC effect is only included in the effective mass fitting, not in the full band structure calculations because the prohibitive computational cost.

Figure 5b shows the parabolic fitting of the band edges to obtain the effective masses, which are intimately related to the carrier transport properties. Note that Figure 5b includes the SOC effect, which tends to significantly reduce the hole effective masses, while has little effect on the electron effective masses (see Figure S5 in the SI). It can be seen that $LaScSe_3$ possesses small effective masses for holes, especially along the Γ-Y direction (0.20 m_0). For the electrons, as the CBM is dominated by the Sc 3d electrons, the effective masses are relatively large. Nevertheless, along the Γ-X direction the value of 0.45 m_0 is reasonably small, giving rise to a relatively balanced transport properties for electrons and holes.

As an optoelectronic material, symmetric doping to both n- and p-types is an important issue that determines their practical applications. Using first-principles calculations to estimate the defect transition levels, we screened the possible dopant elements for $LaScSe_3$. To judge the shallowness of the defect transition levels, we use the criteria that (1) the dopant does not introduce a deep Kohn-Sham level in the band gap in the neutral charge state, which can usually be judged by whether the spin magnetic moment is smaller than 1 μ_B and (2) the atomic structure around the defect does not undergo significant change when the defect charge state is changed from neutral to +1 or −1 state. By satisfying these criteria, the dopants are expected to be a hydrogenic defect with its activation energy mainly determined by the effective masses and dielectric constant. As shown in Figure S6, group-II elements (Ca, Sr or Ba) on the La site are shallow acceptors and group-VII elements (Cl, Br or I) on the Se site are shallow donors. For the case of Ca-on-La and Cl-on-Se, we also employed the HSE functional calculation to confirm that they are shallow dopants. Given these results, doping is expected to be readily achievable for $LaScSe_3$.

4. Conclusion

In summary, we carried out a computational search for selenide perovskites. We propose to employ the phase stability criterion for precise prediction of thermodynamically stable materials. By considering I-V-Se_3, II-IV-Se_3 and III-III-Se_3 compounds, we identified $LaScSe_3$ to be the most possible candidate as the first selenide perovskite free of radiative elements, which is verified by our experiment. The successful prediction of a new material in such an important structure and simple chemical composition suggests a great potential of our approach for discovering new functional inorganic materials. Our HSE, G_0W_0, and BSE calculations including the SOC effect show that $LaScSe_3$ possesses a direct band gap in the green-to-blue region and balanced electron and hole effective masses. Doping to p-type and n-type could be realized by group-II (Ca, Sr and Ba) and group-VII (Cl, Br and I) elements on La and Se sites, respectively. Given these appealing properties, it is expected that the $LaScSe_3$ perovskite is a good optoelectronic material.

ASSOCIATED CONTENT

Supporting Information.

Comparisons of atomic structures of $LaScSe_3$ determined by XRD and DFT calculations and the corresponding XRD patterns, phonon spectra for $LaScSe_3$ at elevated temperatures, projected band structures of $LaScSe_3$ to the constituent elements, calculated imaginary part of the dielectric constant (ε_2) of $LaScSe_3$ by various methods, fitting of effective masses of electrons and holes.

AUTHOR INFORMATION

Corresponding Author

*E-mail: yysun@mail.sic.ac.cn (Yi-Yang Sun), mingchen@mail.sic.ac.cn (Chen Ming)

Notes

The authors declare no competing financial interests.

ACKNOWLEDGMENT

This work is supported by the National Key Research and Development Program of China under Grant No. 2021YFB3500500.

REFERENCES

(1) Jaffe, H. Piezoelectric Ceramics. *J. Am. Chem. Soc.* **1958**, *41* (11), 494–498. https://doi.org/10.1111/j.1151-2916.1958.tb12903.x.

(2) Zhang, S.; Li, F.; Jiang, X.; Kim, J.; Luo, J.; Geng, X. Advantages and Challenges of Relaxor-$PbTiO_3$ Ferroelectric Crystals for Electroacoustic Transducers – A Review. *Prog. Mater. Sci.* **2015**, *68*, 1–66. https://doi.org/10.1016/j.pmatsci.2014.10.002.

(3) Dohner, E. R.; Jaffe, A.; Bradshaw, L. R.; Karunadasa, H. I. Intrinsic White-Light Emission from Layered Hybrid Perovskites. *J. Am. Chem. Soc.* **2014**, *136* (38), 13154–13157. https://doi.org/10.1021/ja507086b.

(4) Luo, J.; Wang, X.; Li, S.; Liu, J.; Guo, Y.; Niu, G.; Yao, L.; Fu, Y.; Gao, L.; Dong, Q.; Zhao, C.; Leng, M.; Ma, F.; Liang, W.; Wang, L.; Jin, S.; Han, J.; Zhang, L.; Etheridge, J.; Wang, J.; Yan, Y.; Sargent, E. H.; Tang, J. Efficient and Stable Emission of Warm-White Light from Lead-Free Halide Double Perovskites. *Nature* **2018**, *563* (7732), 541–545. https://doi.org/10.1038/s41586-018-0691-0.

(5) Stranks, S. D.; Eperon, G. E.; Grancini, G.; Menelaou, C.; Alcocer, M. J. P.; Leijtens, T.; Herz, L. M.; Petrozza, A.; Snaith, H. J. Electron-Hole Diffusion Lengths Exceeding 1 Micrometer

in an Organometal Trihalide Perovskite Absorber. *Science* **2013**, *342* (6156), 341–344. https://doi.org/10.1126/science.1243982.

(6) Bi, D.; Tress, W.; Dar, M. I.; Gao, P.; Luo, J.; Renevier, C.; Schenk, K.; Abate, A.; Giordano, F.; Correa Baena, J.-P.; Decoppet, J.-D.; Zakeeruddin, S. M.; Nazeeruddin, M. K.; Grätzel, M.; Hagfeldt, A. Efficient Luminescent Solar Cells Based on Tailored Mixed-Cation Perovskites. *Sci. Adv.* **2016**, *2* (1), e1501170. https://doi.org/10.1126/sciadv.1501170.

(7) Saliba, M.; Matsui, T.; Domanski, K.; Seo, J.-Y.; Ummadisingu, A.; Zakeeruddin, S. M.; Correa-Baena, J.-P.; Tress, W. R.; Abate, A.; Hagfeldt, A.; Grätzel, M. Incorporation of Rubidium Cations into Perovskite Solar Cells Improves Photovoltaic Performance. *Science* **2016**, *354* (6309), 206–209. https://doi.org/10.1126/science.aah5557.

(8) Correa-Baena, J.-P.; Saliba, M.; Buonassisi, T.; Grätzel, M.; Abate, A.; Tress, W.; Hagfeldt, A. Promises and Challenges of Perovskite Solar Cells. *Science* **2017**, *358* (6364), 739–744. https://doi.org/10.1126/science.aam6323.

(9) Ghosh, S.; Pradhan, B. Lead-Free Metal Halide Perovskite Nanocrystals: Challenges, Applications, and Future Aspects. *ChemNanoMat* **2019**, *5* (3), 300–312. https://doi.org/10.1002/cnma.201800645.

(10) Green, M. A.; Ho-Baillie, A.; Snaith, H. J. The Emergence of Perovskite Solar Cells. *Nat. Photonics* **2014**, *8* (7), 506–514. https://doi.org/10.1038/nphoton.2014.134.

(11) Akkerman, Q. A.; Rainò, G.; Kovalenko, M. V.; Manna, L. Genesis, Challenges and Opportunities for Colloidal Lead Halide Perovskite Nanocrystals. *Nat. Mater.* **2018**, *17* (5), 394–405. https://doi.org/10.1038/s41563-018-0018-4.

(12) Sun, Y.-Y.; Agiorgousis, M. L.; Zhang, P.; Zhang, S. Chalcogenide Perovskites for Photovoltaics. *Nano Lett.* **2015**, *15* (1), 581–585. https://doi.org/10.1021/nl504046x.

(13) Wang, H.; Gou, G.; Li, J. Ruddlesden–Popper Perovskite Sulfides $A_3B_2S_7$: A New Family of Ferroelectric Photovoltaic Materials for the Visible Spectrum. *Nano Energy* **2016**, *22*, 507–513. https://doi.org/10.1016/j.nanoen.2016.02.036.

(14) Niu, S.; Joe, G.; Zhao, H.; Zhou, Y.; Orvis, T.; Huyan, H.; Salman, J.; Mahalingam, K.; Urwin, B.; Wu, J.; Liu, Y.; Tiwald, T. E.; Cronin, S. B.; Howe, B. M.; Mecklenburg, M.; Haiges, R.; Singh, D. J.; Wang, H.; Kats, M. A.; Ravichandran, J. Giant Optical Anisotropy in a Quasi-One-Dimensional Crystal. *Nat. Photonics* **2018**, *12* (7), 392–396. https://doi.org/10.1038/s41566-018-0189-1.

(15) Osei-Agyemang, E.; Adu, C. E.; Balasubramanian, G. Ultralow Lattice Thermal Conductivity of Chalcogenide Perovskite $CaZrSe_3$ Contributes to High Thermoelectric Figure of Merit. *NPJ Comput. Mater.* **2019**, *5* (1), 116. https://doi.org/10.1038/s41524-019-0253-5.

(16) Perera, S.; Hui, H.; Zhao, C.; Xue, H.; Sun, F.; Deng, C.; Gross, N.; Milleville, C.; Xu, X.; Watson, D. F.; Weinstein, B.; Sun, Y.-Y.; Zhang, S.; Zeng, H. Chalcogenide Perovskites – an Emerging Class of Ionic Semiconductors. *Nano Energy* **2016**, *22*, 129–135. https://doi.org/10.1016/j.nanoen.2016.02.020.

(17) Gross, N.; Sun, Y.-Y.; Perera, S.; Hui, H.; Wei, X.; Zhang, S.; Zeng, H.; Weinstein, B. A. Stability and Band-Gap Tuning of the Chalcogenide Perovskite BaZrS3 in Raman and Optical Investigations at High Pressures. *Phys. Rev. Appl.* **2017**, *8* (4), 044014. https://doi.org/10.1103/PhysRevApplied.8.044014.

(18) Niu, S.; Huyan, H.; Liu, Y.; Yeung, M.; Ye, K.; Blankemeier, L.; Orvis, T.; Sarkar, D.; Singh, D. J.; Kapadia, R.; Ravichandran, J. Bandgap Control via Structural and Chemical Tuning of Transition Metal Perovskite Chalcogenides. *Adv. Mater.* **2017**, *29* (9), 1604733. https://doi.org/10.1002/adma.201604733.

(19) Niu, S.; Milam-Guerrero, J.; Zhou, Y.; Ye, K.; Zhao, B.; Melot, B. C.; Ravichandran, J. Thermal Stability Study of Transition Metal Perovskite Sulfides. *J. Mater. Res.* **2018**, *33* (24), 4135–4143. https://doi.org/10.1557/jmr.2018.419.

(20) Hanzawa, K.; Iimura, S.; Hiramatsu, H.; Hosono, H. Material Design of Green-Light-Emitting Semiconductors: Perovskite-Type Sulfide $SrHfS_3$. *J. Am. Chem. Soc.* **2019**, *141* (13), 5343–5349. https://doi.org/10.1021/jacs.8b13622.

(21) Deguchi, T.; Sekiguchi, K.; Nakamura, A.; Sota, T.; Matsuo, R.; Chichibu, S.; Nakamura, S. Quantum-Confined Stark Effect in an AlGaN/GaN/AlGaN Single Quantum Well Structure. *Jpn. J. Appl. Phys.* **1999**, *38* (Part 2, No. 8B), L914–L916. https://doi.org/10.1143/JJAP.38.L914.

(22) Jiang, J.; Chu, Z.; Yin, Z.; Li, J.; Yang, Y.; Chen, J.; Wu, J.; You, J.; Zhang, X. Red Perovskite Light-Emitting Diodes with Efficiency Exceeding 25% Realized by Co-Spacer Cations. *Adv. Mater.* **2022**, *34* (36), 2204460. https://doi.org/10.1002/adma.202204460.

(23) Kim, J. S.; Heo, J.-M.; Park, G.-S.; Woo, S.-J.; Cho, C.; Yun, H. J.; Kim, D.-H.; Park, J.; Lee, S.-C.; Park, S.-H.; Yoon, E.; Greenham, N. C.; Lee, T.-W. Ultra-Bright, Efficient and Stable Perovskite Light-Emitting Diodes. *Nature* **2022**, *611* (7937), 688–694. https://doi.org/10.1038/s41586-022-05304-w.

(24) Liu, S.; Guo, Z.; Wu, X.; Liu, X.; Huang, Z.; Li, L.; Zhang, J.; Zhou, H.; Sun, L.-D.; Yan, C.-H. Zwitterions Narrow Distribution of Perovskite Quantum Wells for Blue Light-Emitting Diodes with Efficiency Exceeding 15%. *Adv. Mater.* **2022**, 2208078. https://doi.org/10.1002/adma.202208078.

(25) Fang, T.; Zhang, F.; Yuan, S.; Zeng, H.; Song, J. Recent Advances and Prospects toward Blue Perovskite Materials and Light-Emitting Diodes. *InfoMat* **2019**, *1* (2), 211–233. https://doi.org/10.1002/inf2.12019.

(26) Gholipour, B.; Müller, M. J.; Li, Y.; Jo, S. S.; Cui, Y.; Mandal, A.; Eggleton, B.; Rochette, M.; Rezaei, M.; Alamgir, I.; Shamim, M. H. M.; Kormokar, R.; Anjum, A.; Zeweldi, G.; Karnik, T. S.; Hu, J.; Kasap, S.; Belev, G.; Reznik, A.; Elliott, S. R.; Wuttig, M.; Hewak, D. W.; Hayden, B.; Jaramillo, R.; Simpson, R. E.; Tominaga, J. Roadmap on Chalcogenide Photonics. *J. Phys. Photonics* **2022**. https://doi.org/10.1088/2515-7647/ac9a91.

(27) Wei, X.; Hui, H.; Zhao, C.; Deng, C.; Han, M.; Yu, Z.; Sheng, A.; Roy, P.; Chen, A.; Lin, J.; Watson, D. F.; Sun, Y.-Y.; Thomay, T.; Yang, S.; Jia, Q.; Zhang, S.; Zeng, H. Realization of $BaZrS_3$ Chalcogenide Perovskite Thin Films for Optoelectronics. *Nano Energy* **2020**, *68*, 104317. https://doi.org/10.1016/j.nanoen.2019.104317.

(28) Sadeghi, I.; Ye, K.; Xu, M.; Li, Y.; LeBeau, J. M.; Jaramillo, R. Making $BaZrS_3$ Chalcogenide Perovskite Thin Films by Molecular Beam Epitaxy. *Adv. Funct. Mater.* **2021**, *31* (45), 2105563. https://doi.org/10.1002/adfm.202105563.

(29) Wei, X.; Hui, H.; Perera, S.; Sheng, A.; Watson, D. F.; Sun, Y.-Y.; Jia, Q.; Zhang, S.; Zeng, H. Ti-Alloying of $BaZrS_3$ Chalcogenide Perovskite for Photovoltaics. *ACS Omega* **2020**, *5* (30), 18579–18583. https://doi.org/10.1021/acsomega.0c00740.

(30) Yu, Z.; Wei, X.; Zheng, Y.; Hui, H.; Bian, M.; Dhole, S.; Seo, J.-H.; Sun, Y.-Y.; Jia, Q.; Zhang, S.; Yang, S.; Zeng, H. Chalcogenide Perovskite $BaZrS_3$ Thin-Film Electronic and Optoelectronic Devices by Low Temperature Processing. *Nano Energy* **2021**, *85*, 105959. https://doi.org/10.1016/j.nanoen.2021.105959.

(31) Rodier, N.; Laruelle, P.; Flahaut, J. Sur Une Nouvelle Serie de Combinaisons Des Sesquisulfures de Terres Rares et d'yttrium Avec Le Sesquisulfure de Scandium. *C. R. Acad. Sc. Paris* **1969**, *C269*, 1391–1393.

(32) Knox, K. Perovskite-like Fluorides. I. Structures of $KMnF_3$, $KFeF_3$, $KNiF_3$ and $KZnF_3$. Crystal Field Effects in the Series and in $KCrF_3$ and $KCuF_3$. *Acta Crystallogr.* **1961**, *14* (6), 583–585. https://doi.org/10.1107/S0365110X61001868.

(33) Noh, J. H.; Im, S. H.; Heo, J. H.; Mandal, T. N.; Seok, S. I. Chemical Management for Colorful, Efficient, and Stable Inorganic–Organic Hybrid Nanostructured Solar Cells. *Nano Lett.* **2013**, *13* (4), 1764–1769. https://doi.org/10.1021/nl400349b.

(34) Edri, E.; Kirmayer, S.; Kulbak, M.; Hodes, G.; Cahen, D. Chloride Inclusion and Hole Transport Material Doping to Improve Methyl Ammonium Lead Bromide Perovskite-Based High Open-Circuit Voltage Solar Cells. *J. Phys. Chem. Lett.* **2014**, *5* (3), 429–433. https://doi.org/10.1021/jz402706q.

(35) Hahn, H.; Mutschke, U. Untersuchungen über ternäre Chalkogenide. XI. Versuche zur Darstellung von Thioperowskiten. *Zeitschrift für Anorg. und Allg. Chemie* **1957**, *288* (5–6), 269–278. https://doi.org/10.1002/zaac.19572880505.

(36) Bergerhoff, G.; Hundt, R.; Sievers, R.; Brown, I. D. The Inorganic Crystal Structure Data Base. *J. Chem. Inf. Comput. Sci.* **1983**, *23* (2), 66–69. https://doi.org/10.1021/ci00038a003.

(37) Noel, H. Selenated Uranium Combinations in USe_2-MSe Systems (M=Mg, Ti, V, Cr, Mn, Fe, Co, Ni). *C. R. Acad. Sc. Paris* **1974**, *C279(12)*, 513–515.

(38) Kresse, G.; Furthmüller, J. Efficiency of Ab-Initio Total Energy Calculations for Metals and Semiconductors Using a Plane-Wave Basis Set. *Computational Materials Science* **1996**, *6* (1), 15–50. https://doi.org/10.1016/0927-0256(96)00008-0.

(39) Kresse, G.; Joubert, D. From Ultrasoft Pseudopotentials to the Projector Augmented-Wave Method. *Phys. Rev. B* **1999**, *59* (3), 1758–1775. https://doi.org/10.1103/PhysRevB.59.1758.

(40) Perdew, J. P.; Ruzsinszky, A.; Csonka, G. I.; Vydrov, O. A.; Scuseria, G. E.; Constantin, L. A.; Zhou, X.; Burke, K. Restoring the Density-Gradient Expansion for Exchange in Solids and Surfaces. *Phys. Rev. Lett.* **2008**, *100* (13), 136406. https://doi.org/10.1103/PhysRevLett.100.136406.

(41) Sun, J.; Ruzsinszky, A.; Perdew, J. P. Strongly Constrained and Appropriately Normed Semilocal Density Functional. *Phys. Rev. Lett.* **2015**, *115* (3), 036402. https://doi.org/10.1103/PhysRevLett.115.036402.

(42) Togo, A.; Tanaka, I. First Principles Phonon Calculations in Materials Science. *Scripta Materialia* **2015**, *108*, 1–5. https://doi.org/10.1016/j.scriptamat.2015.07.021.

(43) Hellman, O.; Abrikosov, I. A.; Simak, S. I. Lattice Dynamics of Anharmonic Solids from First Principles. *Phys. Rev. B* **2011**, *84* (18), 180301. https://doi.org/10.1103/PhysRevB.84.180301.

(44) Petříček, V.; Dušek, M.; Palatinus, L. Crystallographic Computing System JANA2006: General Features. *Z. Kristallogr* **2014**, *229* (5), 345–352. https://doi.org/10.1515/zkri-2014-1737.

(45) Besancon, P.; Laruelle, P. Sur La Variete Alpha Des Sulfures de Terres Rares. *C. R. Acad. Sc. Paris* **1969**, *C48*, 48–53.

(46) Dismukes, J. P.; White, J. G. Rare Earth Sesquiselenides and Sesquitellurides with the Sc_2S_3 Structure. *Inorg. Chem.* **1965**, *4* (7), 970–973. https://doi.org/10.1021/ic50029a010.

(47) Lelieveld, R.; IJdo, D. J. W. Sulphides with the $GdFeO_3$ Structure. *Acta Crystallogr. B* **1980**, *36* (10), 2223–2226. https://doi.org/10.1107/S056774088000845X.

(48) Heyd, J.; Scuseria, G. E.; Ernzerhof, M. Hybrid Functionals Based on a Screened Coulomb Potential. *J. Chem. Phys.* **2003**, *118* (18), 8207–8215. https://doi.org/10.1063/1.1564060.

(49) Hybertsen, M. S.; Louie, S. G. Electron Correlation in Semiconductors and Insulators: Band Gaps and Quasiparticle Energies. *Phys. Rev. B* **1986**, *34* (8), 5390–5413. https://doi.org/10.1103/PhysRevB.34.5390.

(50) Rohlfing, M.; Louie, S. G. Electron-Hole Excitations and Optical Spectra from First Principles. *Phys. Rev. B* **2000**, *62* (8), 4927–4944. https://doi.org/10.1103/PhysRevB.62.4927.